

Circumferential defect detection using ultrasonic guided waves: An efficient quantitative technique for pipeline inspection

Yihui Da¹, Guirong Dong², Bin Wang¹, Dianzi Liu^{3*}, Zhenghua Qian^{1*}

1 State Key Laboratory of Mechanics and Control of Mechanical Structures, College of Aerospace Engineering,

Nanjing University of Aeronautics and Astronautics, Nanjing, China

2 Faculty of High Vocational Education, Xi'an University of Technology, Xi'an, China

3 School of Mathematics, University of East Anglia, Norwich, UK, NR4 7TJ

**Corresponding authors*

E-mail addresses: dianzi.liu@uea.ac.uk (D. Liu), qianzh@nuaa.edu.cn (Z. Qian).

Abstract

With the ability to propagate very long distances, guided waves have been good candidates for serving as an efficient non-destructive evaluation (NDE) method. In this paper, theoretical work is carried out by developing the appropriate dispersion equations for circumferential guided waves in a pipe. Meanwhile, strain formulations are derived from a general equidistant surface coordinate, in which one of axes is parallel to the propagation of waves. Following that, a semi-analytical FEM is adopted to solve the dispersion equations. Then, scattered fields in a circular annulus are calculated using the hybrid FEM and the obtained results are verified by the conservation of energy principle. Finally, the recently developed QDFT (quantitative detection of Fourier transform) technique is further enhanced for the reconstruction of circumferential defects in pipeline structures. Four numerical examples of flaw detection problems are examined to demonstrate the correctness of this technique in terms of accuracy and efficiency. Results show that reconstruction of circumferential surface defects using improved QDFT method can be performed quickly without the necessity of analytical formulations and also streamline the whole procedure of inspecting surface defects, which will lead to the reduced time for practical engineering tests.

Keywords

Surface defect detection, dispersion equations, hybrid FEM, ultrasonic guided waves

1. Introduction

Defect detection in various structures using ultrasonic guided waves has been paid more attention in the field of structural health monitoring (SHE) owing to the accuracy and efficiency of this technique for the inspection. For annulus structures with large radii or thick-walled thicknesses, the motion theory and numerical simulations were applied to analyze the detailed wave propagation by many researches. In early years, Cook and Valkenburg[1] found that the Rayleigh-type wave might propagate along a cylindrical surface. Then, a mathematical model for waves traveling around a solid cylinder immersed in water was presented. Following that, a formal asymptotic theory validated at high frequencies was developed for harmonic Rayleigh surface waves traveling over the general smooth free surface of a homogeneous elastic solid[2]. Recently, the research about guided waves in a circular annulus[3][4] has been focused on the theoretical derivation of dispersion equations and the relationship between a flat plate and an annulus with an infinite radius.

The main step in the traditional inspection process is the calculation of scattered fields, which is defined as solving a forward problem. Rattanawangcharoen[5] combined finite element (FE)

formulations and the wave function expansion to investigate the plane strain wave scattering by cracks in cylinders. Wang et al. [6] simulated the behaviors of circumferential shear horizontal (SH) guided waves using commercial FE software ABAQUS. Based on the results from forward problems, the relationships between scattered fields and defect profiles were determined.

In the meanwhile, ultrasonic guided waves have been used to detect defects in plate-like structures. Leonard et al.[7] applied tomographic reconstruction for nondestructive evaluation (NDE) of aerospace structures. Huthwaite and Simonetti[8] and Huthwaite[9] compared the ray tomography with diffraction tomography techniques and provided a mechanism for determining the thickness from a velocity reconstruction. Luo et al.[10] suggested that circumferential SH waves could be used for the inspection and sizing of axial cracks in pipelines. To generate circumferential shear horizontal guided waves, experiments on two sample pipes having notches with different depths and lengths were carried out utilizing magnetostrictive sensor (MsS) technology. Similarly, SH guided waves propagating in the circumferential direction of pipeline were modeled in 3D and implemented to analyze axial cracking in in-line inspection (ILI) tools[6]. Valle et al.[11] applied guided circumferential waves in a hollow isotropic cylinder to research both the crack location and size, and indicated that the confine of inspecting small cracks with high frequency signals was significantly weakened by the mentioned techniques. Liu et al.[12] proposed a new multichannel time reversal focusing (MTRF) method to detect different kinds of defects in thick-walled pipes with large diameters using circumferential Lamb waves. Liu et al.[13] combined the guided circumferential wave (GCW) with continuous wavelet transform (CWT) to identify radial cracks in pipes. Shivaraj et al.[14] used a higher order cylindrically guided ultrasonic wave for the detection and sizing of hidden pitting-type corrosion in the hidden crevice regions (between the pipe and the pipe supports) without lifting or disturbing the structural layout arrangement of the pipelines. An axial transducer array or a single axially scanned transducer was suggested to send and receive dispersive circumferential guided waves around a pipe[15]. Furthermore, ultrasonic waves sensed through Electro-Magnetic Acoustic Transducer (EMAT) actuators were also utilized to meet the requirements from practical applications[16][17]. Common-source synthetic focusing was used to reconstruct defect images from the guided wave signals, where filters operating in the spectral domain of wavenumber, circumferential order and frequency were designed to suppress the signal components of unwanted mode-family and unwanted traveling direction[18].

However, it has been challenging to complete the quantitative reconstruction of arbitrary surface defects in annulus structures using circumferential guided waves. To address this issue, a novel approach is proposed in this paper to accurately and efficiently achieve the reconstruction of surface defects in such structures. The quantitative detection procedure consists of three parts: the dispersion analysis of circumferential guided waves in a circular annulus, the calculation of scattered fields, and the defect reconstruction using reflection coefficients extracted from scattered fields. First, the dispersion equations have been derived for helix guided waves with an arbitrary incident angle propagating in a hollow cylinder and then solved using the semi-analytical finite element method (SAFEM)[19][20]. The obtained results have been validated by other published data. To calculate scattered fields, the in-house hybrid FEM[21][22] has been developed to numerically determine the scattered fields and its correctness has been verified by the theory of energy conversation. Finally, the developed Quantitative Detection of Fourier Transform (QDFT) approach has been applied to reconstruct four types of surface defects in annulus structures with high levels of accuracy and efficiency.

2. Analysis of dispersion equations for annulus structures

The analysis of guided wave dispersion is of great importance to grasp the propagation mechanism in the structure. It can help to choose optimum modes of guided waves for the defect reconstruction. In this paper, a generalized orthogonal coordinate $(\alpha_1, \alpha_2, \alpha_3)$ shown in Fig.1 has been defined to derive the dispersion equations of helical guided waves traveling in a hollow cylinder so that the circumferential guided waves can be represented by assigning the value of zero to the incident angle θ . For helical guided waves propagate with an arbitrary angle θ in a hollow cylinder, the curvatures for the geodesics[23] which are spirals for the surface of the hollow cylinder can be expressed as

$$\tilde{\kappa}_1 = \kappa_1 \cos^2 \theta + \kappa_2 \sin^2 \theta, \quad \tilde{\kappa}_2 = \kappa_1 \sin^2 \theta + \kappa_2 \cos^2 \theta \quad (1)$$

where $\kappa_1 = 1/r_{\text{out}}$ and $\kappa_2 = 0$, which are the principal curvatures of the outside surface defined in a cylindrical system. The curvatures of the coordinate α_1 and α_2 are denoted as $\tilde{\kappa}_1$ and $\tilde{\kappa}_2$, respectively. Hence, Lamé coefficients (scale factors) can be written as, where the outsider surface is considered as the reference surface of equidistant surface,

$$h_1 = 1 + \tilde{\kappa}_1 \alpha_3, \quad h_2 = 1 + \tilde{\kappa}_2 \alpha_3, \quad h_3 = 1 \quad (2)$$

Thus, the relationship between the particle displacements u_i and strains ε_{ij} are represented as

$$\begin{aligned} \varepsilon_{11} &= \frac{1}{h_1} \frac{\partial u_1}{\partial \alpha_1} + \frac{\tilde{\kappa}_1}{h_1} u_3, \quad \varepsilon_{22} = \frac{1}{h_2} \frac{\partial u_2}{\partial \alpha_2} + \frac{\tilde{\kappa}_2}{h_2} u_3, \quad \varepsilon_{33} = \frac{\partial u_3}{\partial \alpha_3} \\ \varepsilon_{12} &= \frac{1}{2} \left(\frac{1}{h_1} \frac{\partial u_2}{\partial \alpha_1} + \frac{1}{h_2} \frac{\partial u_1}{\partial \alpha_2} \right), \quad \varepsilon_{13} = \frac{1}{2} \left(\frac{1}{h_1} \frac{\partial u_3}{\partial \alpha_1} + \frac{\partial u_1}{\partial \alpha_3} - \frac{\tilde{\kappa}_1}{h_1} u_1 \right), \quad \varepsilon_{23} = \frac{1}{2} \left(\frac{1}{h_2} \frac{\partial u_3}{\partial \alpha_2} + \frac{\partial u_2}{\partial \alpha_3} - \frac{\tilde{\kappa}_2}{h_2} u_2 \right) \end{aligned} \quad (3)$$

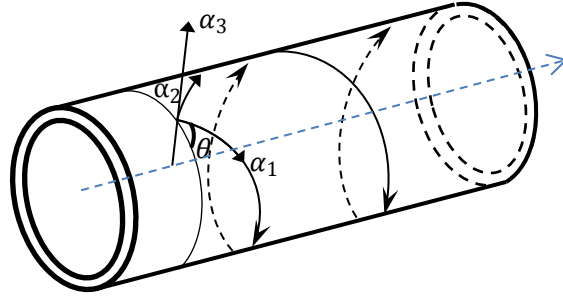


Fig. 1 Helical guided waves propagating along α_1 direction in a pipe

Eq.(3) can be written in matrix form as follows

$$\boldsymbol{\varepsilon} = \begin{bmatrix} \frac{1}{h_1} \frac{\partial}{\partial \alpha_1} & 0 & \frac{\tilde{\kappa}_1}{h_1} \\ 0 & \frac{1}{h_2} \frac{\partial}{\partial \alpha_2} & \frac{\tilde{\kappa}_2}{h_2} \\ 0 & 0 & \frac{\partial}{\partial \alpha_3} \\ 0 & \frac{\partial}{\partial \alpha_3} - \frac{1}{h_2} \frac{\partial}{\partial \alpha_2} & \frac{1}{h_2} \frac{\partial}{\partial \alpha_2} \\ \frac{\partial}{\partial \alpha_3} - \frac{1}{h_1} \frac{\partial}{\partial \alpha_1} & 0 & \frac{1}{h_1} \frac{\partial}{\partial \alpha_1} \\ \frac{1}{h_2} \frac{\partial}{\partial \alpha_2} & \frac{1}{h_1} \frac{\partial}{\partial \alpha_1} & 0 \end{bmatrix} \begin{bmatrix} u_1 \\ u_2 \\ u_3 \end{bmatrix} = \mathbf{L} \mathbf{u} \quad (4)$$

where

$$\mathbf{L} = \mathbf{L}_1 \frac{1}{h_1} \frac{\partial}{\partial \alpha_1} + \mathbf{L}_2 \frac{1}{h_2} \frac{\partial}{\partial \alpha_2} + \mathbf{L}_3 \frac{\partial}{\partial \alpha_3} + \mathbf{L}_4 \frac{\tilde{\kappa}_1}{h_1} + \mathbf{L}_5 \frac{\tilde{\kappa}_2}{h_2}$$

$$\mathbf{L}_1 = \begin{bmatrix} 1 & 0 & 0 \\ 0 & 0 & 0 \\ 0 & 0 & 0 \\ 0 & 0 & 1 \\ 0 & 1 & 0 \end{bmatrix}, \mathbf{L}_2 = \begin{bmatrix} 0 & 0 & 0 \\ 0 & 1 & 0 \\ 0 & 0 & 0 \\ 0 & 0 & 1 \\ 1 & 0 & 0 \end{bmatrix}, \mathbf{L}_3 = \begin{bmatrix} 0 & 0 & 0 \\ 0 & 0 & 0 \\ 0 & 0 & 1 \\ 0 & 1 & 0 \\ 1 & 0 & 0 \\ 0 & 0 & 0 \end{bmatrix}, \mathbf{L}_4 = \begin{bmatrix} 0 & 0 & 1 \\ 0 & 0 & 0 \\ 0 & 0 & 0 \\ 0 & 0 & 0 \\ -1 & 0 & 0 \\ 0 & 0 & 0 \end{bmatrix}, \mathbf{L}_5 = \begin{bmatrix} 0 & 0 & 0 \\ 0 & 0 & 1 \\ 0 & 0 & 0 \\ 0 & -1 & 0 \\ 0 & 0 & 0 \\ 0 & 0 & 0 \end{bmatrix} \quad (5)$$

Along the wall thickness (the direction of α_3), the hollow cylinder is discretized so that the displacements are represented as:

$$\mathbf{u}(\alpha_1, \alpha_2, \alpha_3) = [u_1 \quad u_2 \quad u_3]^T = \mathbf{N}(\alpha_3) \mathbf{U}(\alpha_1, \alpha_2) \quad (6)$$

where \mathbf{N} is a matrix of element shape function.

Substituting Eqs. (5) and (6) into Eq.(4), the strains are denoted as

$$\boldsymbol{\varepsilon} = \mathbf{L} \mathbf{u} = \mathbf{L}_1 \frac{1}{h_1} \mathbf{N} \mathbf{U}_{,1} + \mathbf{L}_2 \frac{1}{h_2} \mathbf{N} \mathbf{U}_{,2} + \mathbf{L}_3 \mathbf{N}_{,3} \mathbf{U} + \mathbf{L}_4 \frac{\tilde{\kappa}_1}{h_1} \mathbf{N} \mathbf{U} + \mathbf{L}_5 \frac{\tilde{\kappa}_2}{h_2} \mathbf{N} \mathbf{U} \quad (7)$$

Applying Fourier series, the displacements \mathbf{U} in the direction α_2 can be written as

$$\mathbf{U}(\alpha_1, \alpha_2) = \sum_{n=-\infty}^{+\infty} e^{in\alpha_2} \mathbf{U}_n(\alpha_1) \quad (8)$$

where $\mathbf{U}_n(\alpha_1) = \int \bar{\mathbf{U}}_n(\xi_n) e^{i\xi_n \alpha_1} d\xi_n$ employing Fourier transform and ξ_n represents a wavenumber.

According to Hamilton's principle, the governing equations can be given

$$[\mathbf{A}(n, \omega) - \xi_n \mathbf{B}(n, \omega)] \mathbf{Q}_n = \mathbf{P}_n,$$

$$\mathbf{A} = \begin{bmatrix} \mathbf{0} & \mathbf{W} + \mathbf{M}_3 \\ \mathbf{W} + \mathbf{M}_3 & \mathbf{M}_2 \end{bmatrix}, \mathbf{B} = \begin{bmatrix} \mathbf{W} + \mathbf{M}_3 & \mathbf{0} \\ \mathbf{0} & -\mathbf{M}_1 \end{bmatrix} \quad (9)$$

where

$$\mathbf{B}_1 = \mathbf{L}_1 \frac{1}{h_1} \mathbf{N}, \mathbf{B}_2 = \mathbf{L}_2 \frac{1}{h_2} \mathbf{N}, \mathbf{B}_3 = \mathbf{L}_3 \mathbf{N}_{,3} + \mathbf{L}_4 \frac{\tilde{\kappa}_1}{h_1} \mathbf{N} + \mathbf{L}_5 \frac{\tilde{\kappa}_2}{h_2} \mathbf{N},$$

$$\mathbf{M}_1 = \int \mathbf{B}_1^T \mathbf{D} \mathbf{B}_1 h_1 h_2 d\alpha_3, \mathbf{M}_2 = \int [i \mathbf{B}_3^T \mathbf{D} \mathbf{B}_1 - i \mathbf{B}_1^T \mathbf{D} \mathbf{B}_3 + n \tilde{\kappa}_2 \mathbf{B}_2^T \mathbf{D} \mathbf{B}_1 + n \tilde{\kappa}_2 \mathbf{B}_1^T \mathbf{D} \mathbf{B}_2] h_1 h_2 d\alpha_3,$$

$$\mathbf{M}_3 = \int [in \tilde{\kappa}_2 \mathbf{B}_3^T \mathbf{D} \mathbf{B}_2 - in \tilde{\kappa}_2 \mathbf{B}_2^T \mathbf{D} \mathbf{B}_3 + (n \tilde{\kappa}_2)^2 \mathbf{B}_2^T \mathbf{D} \mathbf{B}_2 + \mathbf{B}_3^T \mathbf{D} \mathbf{B}_3] h_1 h_2 d\alpha_3,$$

$$\mathbf{W} = \int (-\omega^2 \rho \mathbf{N}^T \mathbf{N}) h_1 h_2 d\alpha_3, \mathbf{Q}_n = [\bar{\mathbf{U}}_n \quad \xi_n \bar{\mathbf{U}}_n]^T, \mathbf{P}_n = [\mathbf{0} \quad \bar{\mathbf{F}}_n]^T \quad (10)$$

ω and ρ are the circular frequency and the material density; $\bar{\mathbf{U}}_n$ represents displacements in the wavenumber domain, which are obtained by inverse Fourier transform of $\mathbf{U}_n(\alpha_1)$ in Eq.(8); and $\bar{\mathbf{F}}_n$ is the loads in the wavenumber domain and its definition is the same as $\bar{\mathbf{U}}_n$. In order to obtain the nontrivial solutions of the dispersion equations, the determinant of the matrix in Eq.(9) should be equal to zero as follows:

$$|\mathbf{A}(n, \omega) - \xi_n \mathbf{B}(n, \omega)| = 0 \quad (11)$$

Solving the Eq.(11), the left eigenvectors $\boldsymbol{\phi}_{nm}^L$ and right eigenvectors $\boldsymbol{\phi}_{nm}^R$ are obtained as functions of different eigenvalues k_{nm} (wavenumber), in which the subscript m means the order number of guided wave modes and n represents the order number for the axis α_2 . Then, based on Zhuang's work[19], the displacement and stress formulas (\mathbf{U}_n and $\boldsymbol{\sigma}_n$) are derived as

$$\mathbf{U}_n = -\frac{i k_{nm} [\boldsymbol{\phi}_{nm}^L]^H \mathbf{P}_n}{2\pi B_{nm}} \boldsymbol{\phi}_{nm}^R e^{-ik_{nm}(\alpha_1 - \alpha_0)} = \boldsymbol{\Phi}_{nm} e^{-ik_{nm}(\alpha_1 - \alpha_0)} \quad (12)$$

$$\sigma_n = \left\{ \mathbf{D} [(\mathbf{B}_1 + in\tilde{\kappa}_2\mathbf{B}_2 - ik_{nm}\mathbf{B}_3)\Phi_{nm}] \right\} e^{-ik_{nm}(\alpha_1 - \alpha_0)} = \mathbf{t}_n e^{-ik_{nm}(\alpha_1 - \alpha_0)}$$

where α_0 is the position of load \mathbf{P}_n in axis α_1 , \mathbf{D} represents elastic moduli matrix.

Based on the aforementioned semi-analytical finite element (SAFE) method, the dispersion equations of helix guided waves in pipes can be numerically solved to discover the relationship between the frequency and the wave phase velocity using the examples as follows:

In the numerical tests, material properties and the geometry of a pipe has been given in Table 1. In Fig.2, different incident angles $\theta = 0, \pi/6, \pi/4, \pi/3, \pi/2$ have been selected to calculate the corresponding dispersion curves of the plane mode waves and the superscript ‘ \sim ’ represents the anti-plane mode. It is emphasized that in this paper the situation of the order number $n = 0$ is considered. When $\theta = \pi/2$, the guided waves propagate along the axis of the cylinder and for the incident angle $\theta = 0$, the circumferential guided waves can be obtained. In the cases with the incident angles $\theta = \pi/6, \pi/4, \pi/3$, it can be observed that the propagation paths of guided waves are helix curves, which make the problem more difficult for the calculation of scattered fields caused by structural flaws. In this paper, the outer wall of the hollow cylinder is considered as the reference surface. Unless otherwise stated, wavenumbers and phase velocities correspond to the values at the outer surface. When the incident angle θ is decreased from $\pi/2$ to 0, the phase velocity gradually become larger. This can be also proved in three different cases: $r_{in}/r_{out} = 0.1$, $r_{in}/r_{out} = 0.5$, and $r_{in}/r_{out} = 0.95$ shown in Fig.3. The obtained solutions have a good agreement with the results by Liu [3]. As r_{in}/r_{out} is increased, the 0th plane mode fades away and a dispersive to non-dispersive transition of the 1st anti-plane mode can be observed as well as the phase velocity being a little larger than the velocity of transverse waves.

Table 1

Material properties of the pipe model

Density ($\rho, \text{kg/m}^3$)	Inner radius (r_{in} , ,m)	Outer radius (r_{out}, m)	Wall thickness ($h = r_{out} - r_{in}, \text{m}$)	Lame constants (λ and μ, Pa)
8.2324×10^3	3.881×10^{-2}	4.440×10^{-2}	5.590×10^{-3}	1.0878×10^{11} and 8.4302×10^{10}

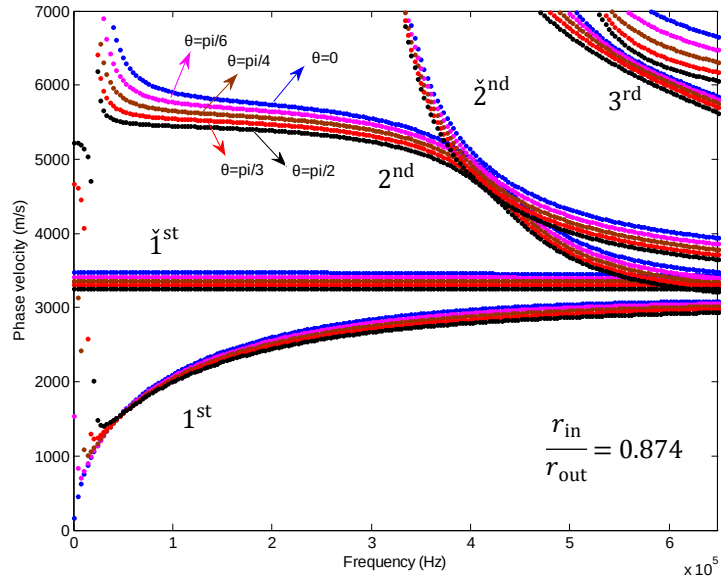


Fig. 2 The dispersion curves of guided waves in pipes with different incident angles

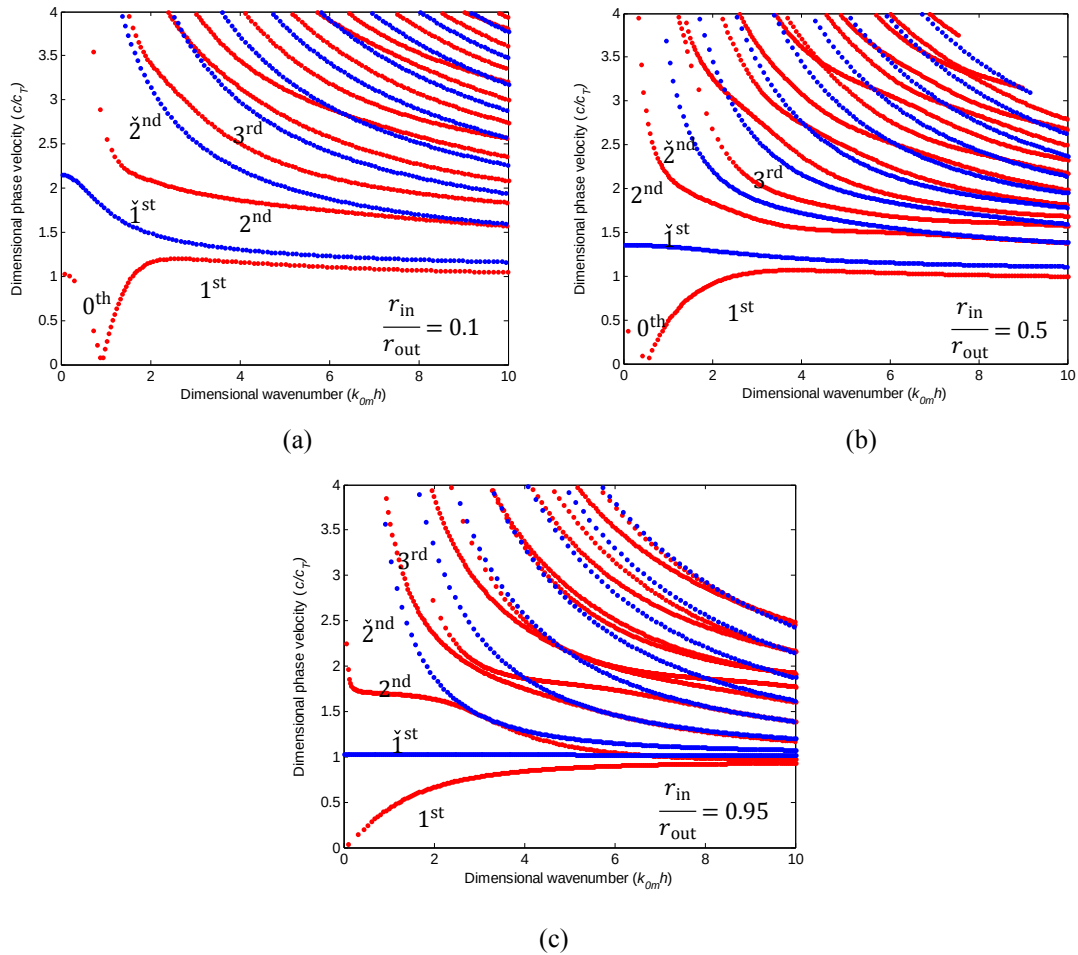


Fig. 3 The dispersion curves of guided waves in pipes with different values of thickness wall, as incident angle $\theta = 0$: (a) $r_{in}/r_{out} = 0.1$; (b) $r_{in}/r_{out} = 0.5$; (c) $r_{in}/r_{out} = 0.95$

In the meanwhile, an example with the ratio $r_{in}/r_{out} = 0.874$ has been examined to compare the results of guided wave modes in circular annulus with the ones in plate shown in Fig.4. The phase

velocity of the $\check{1}^{\text{st}}$ anti-plane mode wave in circular annulus is larger than the one in plate, the cut-off frequency of the 2^{nd} plane mode wave in circular annulus is not equal to zero, and velocities of all plane modes waves in plate are smaller by comparison of the results in circular annulus. It is also noted that the non-dispersive characteristic of the $\check{1}^{\text{st}}$ anti-plane mode wave is remarkable and that is why this mode is used to detect flaws in a circular annulus.

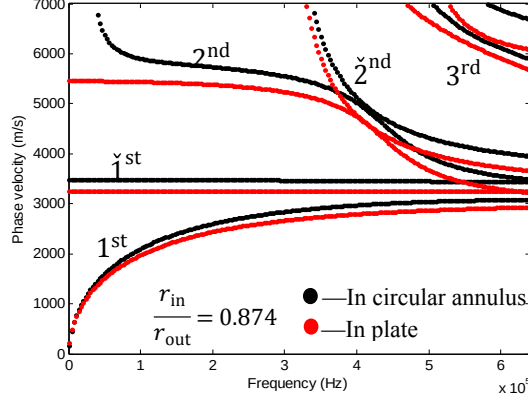


Fig. 4 The dispersion curves of guided waves in circular annulus and in plate

3. Calculation of scattered fields using hybrid FEM

Many three-dimensional engineering simulations can be simplified into a plain strain analysis for computational efficiency. Taking into account this situation, a long pipe with defects that has a constant cross section is investigated for the numerical determination of displacement and stress fields using hybrid FEM in this paper. The circumferential guided waves are adopted to detect flaws in the structure and the circular annulus is represented by a two-dimensional model shown in Fig.5.

For the circumferential wave with the incident angle $\theta = 0$, Eq.(1) can be rewritten as

$$\tilde{\kappa}_1 = \kappa_1, \tilde{\kappa}_2 = 0 \quad (13)$$

where κ_1 mean the curvature.

The whole circular annulus has been divided into two parts shown in Fig.5: one bounded between two cross-sections S_1 and S_2 includes defects (highlighted in red lines), and the other contains the remaining structure. Based on the observation in Fig.4, the $\check{1}^{\text{st}}$ anti-plane mode waves can propagate in a constant phase velocity. Therefore, in this research the clockwise $\check{1}^{\text{st}}$ anti-plane mode guided waves are generated and will travel on the surface of the circular annulus.

It is obvious that the incident and reflected waves propagate through S_2 whilst the transmitted waves travel through S_1 . The nodal displacements and forces of the two cross-sections S_1 and S_2 consist of infinite components induced by different mode waves with unknown amplitudes, which are depicted in *Section 2*. However, most of the non-propagating modes will quickly die off and only the propagating waves and a few non-propagating modes will be used to calculate the scattered fields. Based on authors' previous work[21], the hybrid FEM[22] is implemented to numerically determine the scattered fields of annulus structures with circumferential defects as follows:

The main motion equation is formulated by

$$[\mathbf{G}] \begin{bmatrix} \mathbf{q}_I \\ \tilde{\mathbf{A}} \end{bmatrix} = [\mathbf{T}] \quad (14)$$

$$\text{where } \mathbf{G} = \left\{ \begin{bmatrix} \mathbf{I} & \mathbf{0} \\ \mathbf{0} & [\tilde{\Phi}]^H \end{bmatrix} \begin{bmatrix} \mathbf{S}_{II} & \mathbf{S}_{IB} \\ \mathbf{S}_{BI} & \mathbf{S}_{BB} \end{bmatrix} \begin{bmatrix} \mathbf{I} & \mathbf{0} \\ \mathbf{0} & \tilde{\Phi} \end{bmatrix} - \begin{bmatrix} \mathbf{I} & \mathbf{0} \\ \mathbf{0} & [\tilde{\Phi}]^H \end{bmatrix} \begin{bmatrix} \mathbf{0} & \mathbf{0} \\ \mathbf{0} & \tilde{\mathbf{t}} \end{bmatrix} \right\},$$

$$\mathbf{T} = \begin{bmatrix} \mathbf{I} & \mathbf{0} \\ \mathbf{0} & [\tilde{\Phi}]^H \end{bmatrix} \left\{ \begin{bmatrix} 0 \\ \tilde{\mathbf{t}}^1 \end{bmatrix} - \begin{bmatrix} \mathbf{S}_{11} & \mathbf{S}_{1B} \\ \mathbf{S}_{B1} & \mathbf{S}_{BB} \end{bmatrix} \begin{bmatrix} 0 \\ \tilde{\Phi}^1 \end{bmatrix} \right\}, \quad \tilde{\mathbf{A}} = \begin{bmatrix} \tilde{A}_{01}^{\text{tra}} \\ \vdots \\ \tilde{A}_{0M}^{\text{tra}} \\ \tilde{A}_{01}^{\text{ref}} \\ \vdots \\ \tilde{A}_{0M}^{\text{ref}} \end{bmatrix}, \quad \tilde{\Phi} = [\tilde{\Phi}_{01}^{\text{tra}} \quad \dots \quad \tilde{\Phi}_{0M}^{\text{tra}} \quad \tilde{\Phi}_{01}^{\text{ref}} \quad \dots \quad \tilde{\Phi}_{0M}^{\text{ref}}], \quad \tilde{\Phi}^1$$

$$= \begin{bmatrix} \tilde{\Phi}_{0m}^1 \\ \tilde{\Phi}_{0m}^2 \\ \tilde{\Phi}_{0m} \end{bmatrix}, \quad \tilde{\mathbf{t}}^1 = \begin{bmatrix} \mathbf{t}_{0m}^1 \\ \mathbf{t}_{0m}^2 \\ \mathbf{t}_{0m} \end{bmatrix}, \quad \tilde{\mathbf{t}} = [\tilde{\mathbf{t}}_{01}^{\text{tra}} \quad \dots \quad \tilde{\mathbf{t}}_{0M}^{\text{tra}} \quad \tilde{\mathbf{t}}_{01}^{\text{ref}} \quad \dots \quad \tilde{\mathbf{t}}_{0M}^{\text{ref}}], \quad \mathbf{I} \text{ is an identity matrix, the subscripts I}$$

and B mean interior nodes and boundary nodes, \mathbf{q}_I is the displacement vector of the interior nodes, \tilde{M} is the total number of non-propagating waves and guided waves corresponding to different frequencies, $\tilde{\mathbf{A}}$ is the modified coefficients for scattered fields, $\tilde{\Phi}$ and $\tilde{\mathbf{t}}$ denote nodal displacements and forces induced by a unity amplitude of reflected and transmitted waves propagating through the cross sections S_1 and S_2 , and $\tilde{\Phi}^1$ and $\tilde{\mathbf{t}}^1$ represent nodal displacements and forces incident waves through the cross sections.

Based on the formulations derived in *section 2*, the displacements $\tilde{\Phi}$ and forces $\tilde{\mathbf{t}}$ can be further written as:

$$\tilde{\Phi}_{0m}^{\text{tra}} = \Phi_{0m}^{\text{tra}} e^{-ik_{0m}(s_1\alpha_1 - l\alpha_1)} = -\frac{i k_{0m} [\phi_{0mu}^L]^H \mathbf{P}_0}{2\pi B_{0m}} \phi_{0mu}^R e^{-ik_{0m}(s_1\alpha_1 - l\alpha_1)},$$

$$\tilde{\mathbf{t}}_{0m}^{\text{tra}} = \left\{ \mathbf{D}[(\mathbf{B}_1 - ik_{0m}\mathbf{B}_3)\Phi_{0m}^{\text{tra}}] \right\} e^{-ik_{0m}(s_1\alpha_1 - l\alpha_1)} = \mathbf{t}_0 e^{-ik_{0m}(s_1\alpha_1 - l\alpha_1)},$$

$$m = 1, 2, \dots, \tilde{M}$$
(15)

and

$$\tilde{\Phi}_{0m}^{\text{ref}} = \Phi_{0m}^{\text{ref}} e^{ik_{0m}(s_2\alpha_1 - r\alpha_1)} = -\frac{i k_{0m} [\phi_{0mu}^L]^H \mathbf{P}_0}{2\pi B_{0m}} \phi_{0mu}^R e^{ik_{0m}(s_2\alpha_1 - r\alpha_1)},$$

$$\tilde{\mathbf{t}}_{0m}^{\text{ref}} = \left\{ \mathbf{D}[(\mathbf{B}_1 - ik_{0m}\mathbf{B}_3)\Phi_{0m}^{\text{ref}}] \right\} e^{ik_{0m}(s_2\alpha_1 - r\alpha_1)} = \mathbf{t}_0 e^{ik_{0m}(s_2\alpha_1 - r\alpha_1)},$$

$$m = 1, 2, \dots, \tilde{M}$$
(16)

where $s_1\alpha_1$ and $s_2\alpha_1$ represent circumferential coordinates along the axis α_1 at the truncated left and right cross sections S_1 and S_2 ; $l\alpha_1$ and $r\alpha_1$ denote circumferential coordinates of the left and right boundaries of the defect. More details about the calculation of scattered fields using hybrid FEM can be found in [21].

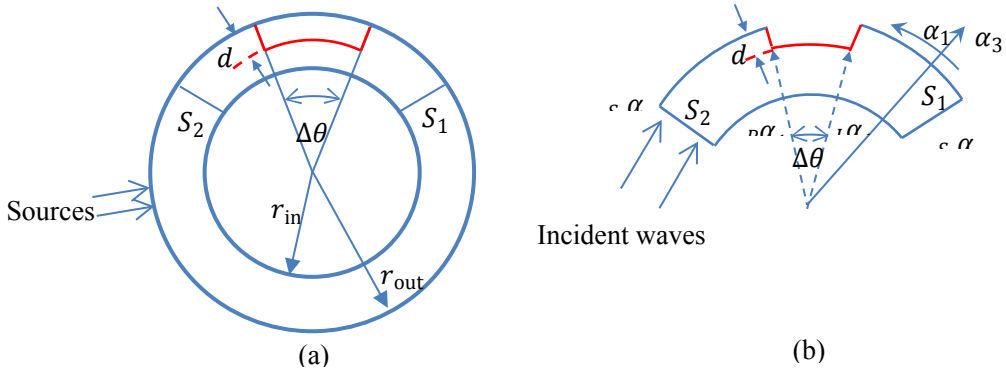


Fig. 5 A circular annulus with a surface defect: (a) Entire vision of schematic and (b) Partial schematic

To demonstrate the correctness of the developed hybrid FEM for the calculation of the scattered fields, numerical simulations of a circular structure with a surface defect shown in Fig.5 have been performed in terms of conservation of energy. It is noted that material properties used in *section 2* have been applied in the following examples. The incident signal frequency range of the mode $\check{1}^{\text{st}}$ guided waves from 0~683.70KHz includes 112 frequency points.

In Case 1, four models are marked as A1, A2, A3 and A4, respectively, in Table 2. The opening angles $\Delta\theta$ of the defects are same ($\Delta\theta = 0.250\text{rad}$). The reflection coefficients calculated by the hybrid FEM are shown in Fig.6. It is obvious that the absolute values of the reflection coefficients increase with the defect depths in the whole frequency range. Especially, when the frequency is lower than about 300.0KHz, the values from model A1 to model A4 are almost linear increase, and there are only two peaks in this frequency range. However, when the frequency is higher than 300.0KHz, the reflection coefficient curves for the different models have their respective shapes. It can be explained by the change of the mode number of anti-plane guided waves, due to cut-off frequency of the mode $\check{2}^{\text{nd}}$ guided waves near 300.0KHz, i. e., when incident frequencies are larger than 300.0KHz, the scattered waves include no longer the $\check{1}^{\text{st}}$ guided waves. From an energy point of view, results of the transmitted energy at the cross section S_1 and reflected energy at the cross section S_2 have been given in Fig.7. The dash lines and solid lines denote the ratios of transmitted and reflected energy to the incident energy flux, respectively. It is obvious that the summation must be equal to 1, according to the law of conservation of energy. Since the two curves are symmetric with respect to the axis whose label (the energy ratio) is 0.5, which explain our simulations are accord to the energy conservation. So it is correct that using the hybrid FEM solves the scattered fields in circular annulus.

In Table 2, another set of four models with different opening angles has been analyzed and labelled as E1, E2, E3 and E4 for each model. The changes in reflection coefficients of different models with frequency can be observed in Fig.8. Obviously, the similar conclusions can be drawn as the findings in Case 1. Summarily, more modes of guided waves will make inspection more complex as the frequency increases. The defect depth mainly affects the amplitudes of the reflection coefficients and the defect length influences the number of peaks of the reflection coefficient curves.

Table 2

The notch sizes in the annulus

	Serial number	A1	A2	A3	A4
Case 1	the depth d	$h/6$	$h/3$	$h/2$	$2h/3$
	the opening angle $\Delta\theta$	0.250rad	0.250rad	0.250rad	0.250rad
	Serial number	E1	E2	E3	E4
Case 2	the depth d	$h/3$	$h/3$	$h/3$	$h/3$
	the opening angle $\Delta\theta$	0.1250rad	0.250rad	0.3750rad	0.50rad

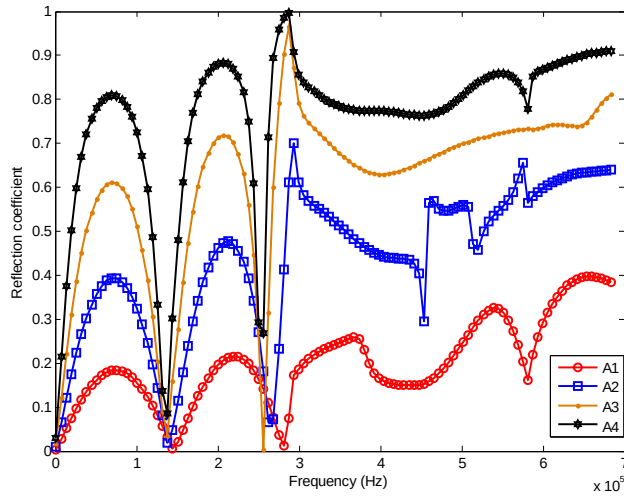


Fig. 6 The mode $\check{1}^{\text{st}}$ reflection coefficients with the same mode incident waves for Case 1

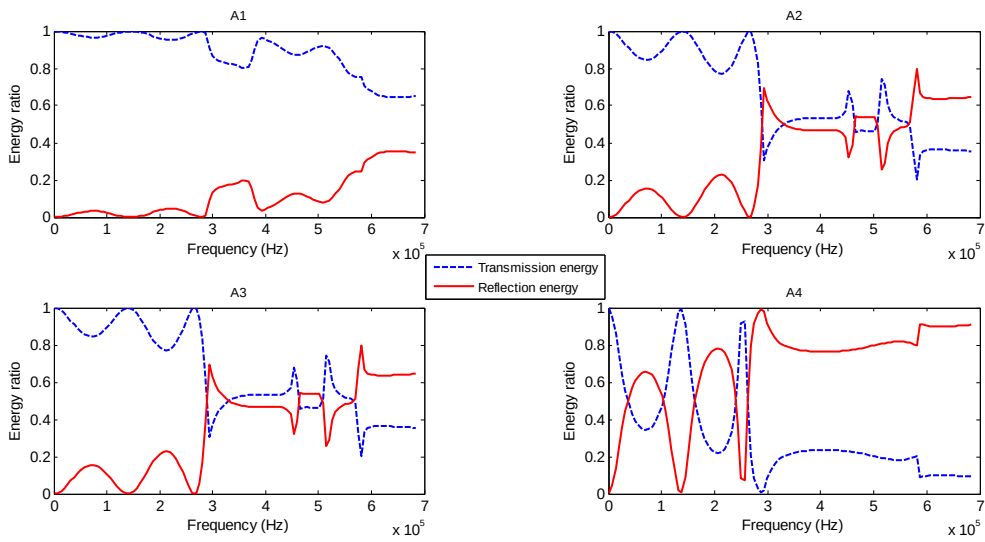


Fig. 7 The energy conservation with the mode $\check{1}^{\text{st}}$ incident waves for Case 1

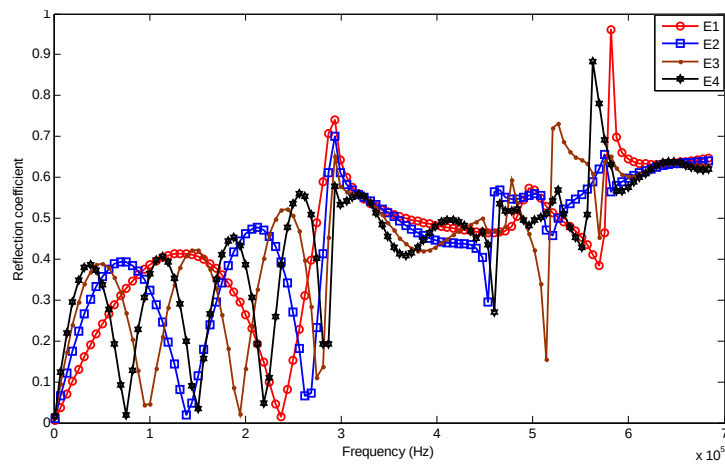


Fig. 8 The mode $\check{1}^{\text{st}}$ reflection coefficients with the same mode incident waves for Case 2

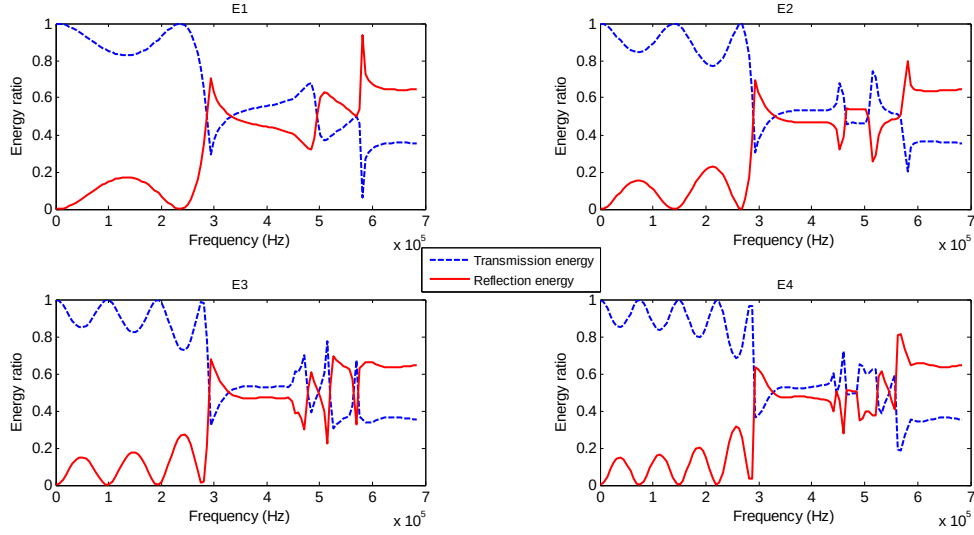


Fig. 9 The energy conservation with the mode $\check{1}^{\text{st}}$ incident waves for Case 2

4. Examples of surface defect reconstruction using extended QDFT method

Based on our previous work, the QDFT (quantitative detection of Fourier transform) approach has been further developed to efficiently reconstruct the defects in the circular annulus, which have been widely used in ocean engineering [24][25]. The flowchart of QDFT has been given in Fig.10 for the detailed procedure of defect detection. Two important stages in this procedure include the calculation of reflection coefficients introduced in *section 3* and the correction of integral coefficients below. More detailed information about QDFT can be found in [21].

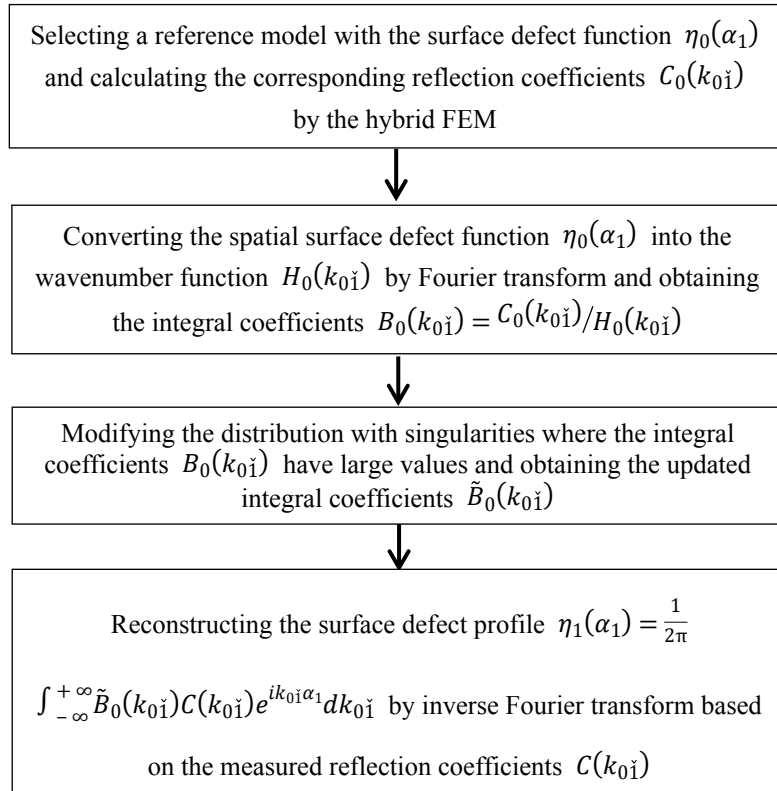


Fig. 10 The procedure of reconstructing surface defects in circular annulus by QDFT

Two reference models (Model 1 and Model 2) shown in Fig.11 and Fig.12 are selected to reconstruct surface defects using the aforementioned QDFT approach. The frequency-dependent reflection and integral coefficients are shown in Fig.13. In order to reduce the influence of singularities of the integral coefficients $B_0(k_{0i})$ on the reconstruction results, a practical strategy is proposed in this paper stating the value of $B_0(k_{0i})$ in the zones including singular points should be assigned to the value of zero for real number or minimal modulus for complex number. In an example shown in Fig.14, where $B_0(k_{0i})$ of the Model 1 is used to reconstruct the defect in the Model 2, the large amplitude fluctuation of reconstruction results is remarkably observed in the no-defect region due to the influence of singularities of integral coefficients $B_0(k_{0i})$. This will deteriorate the accuracy of reconstruction of defects. By Fourier transform, the results in frequency domain are given in Fig.15. It is noted that the peak value locates at about 209.0KHz, which is the frequency for the corresponding singularity in the integral coefficient curve represented by the red line in Fig.13 (b). Thus, the conclusion is drawn that the singularity of $B_0(k_{0i})$ will mainly contribute to the overall fluctuation in the process of defect reconstruction. To enhance the accuracy of the reconstruction result, it is necessary to modify the values of $B_0(k_{0i})$ in the reference model using the proposed strategy. Once the integral coefficients $\tilde{B}_0(k_{0i})$ is updated, the corrected reconstruction result is shown in Fig.16. Obviously, the fluctuation in the no-defect region is effectively suppressed and the accuracy of reconstruction of circumferential defects is significantly improved. Therefore, the proposed strategy for modifying integral coefficients $\tilde{B}_0(k_{0i})$ is employed in the following numerical experiments.

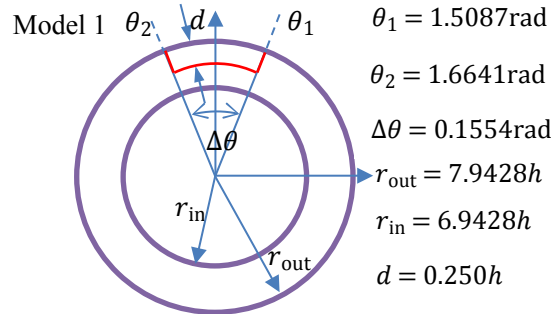


Fig. 11 The sketch of the reference model 1

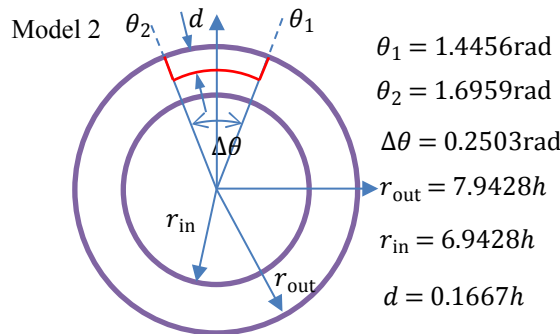


Fig. 12 The sketch of the reference model 2

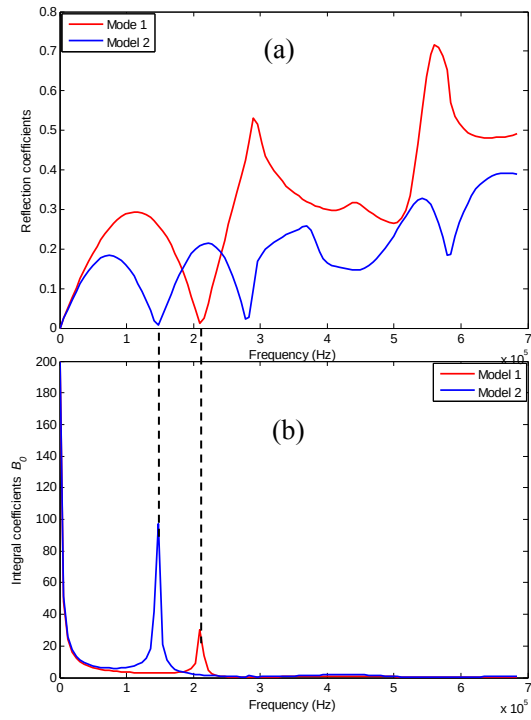


Fig. 13 The reflection coefficients (a) and integral coefficients (b) of the two reference models

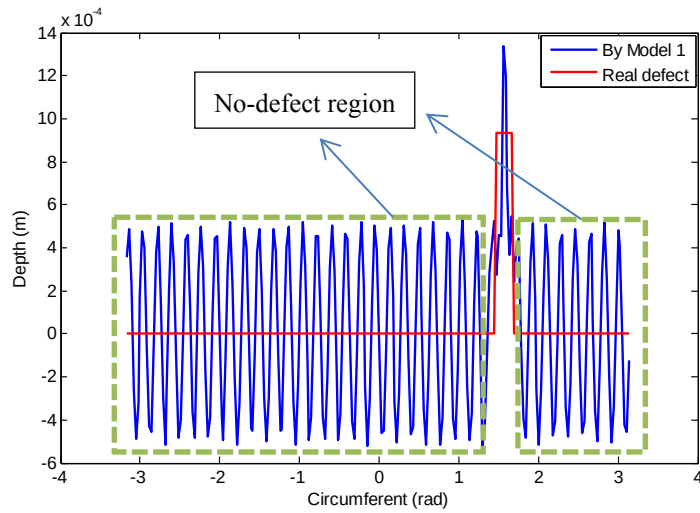


Fig. 14 The reconstructed result based on unprocessed $B_0(k_{0i})$ from the Model 1

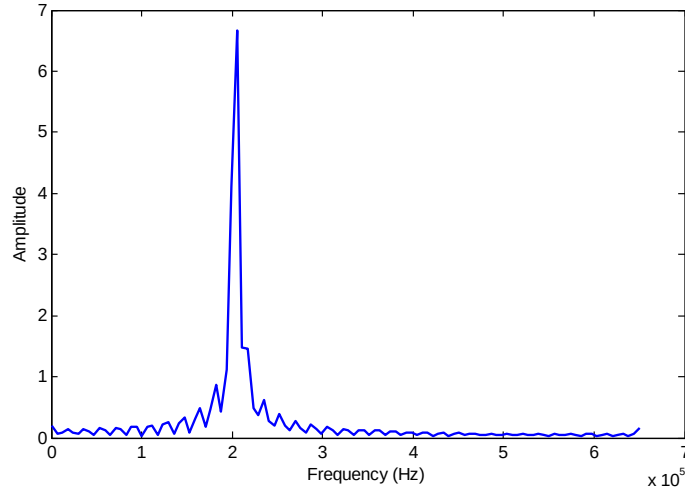


Fig. 15 The result in frequency domain of fluctuations in the no-defect region from Fig.14

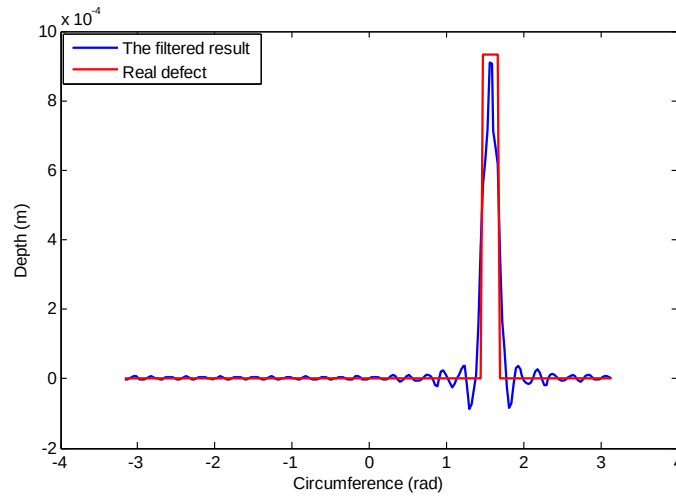


Fig. 16 The reconstruction result based on modified $\tilde{B}_0(k_{0i})$ from the Model 1

In order to demonstrate the superiority of the proposed QDFT approach for arbitrary surface defect detections, reconstructions of different profiles of circumferential defects are performed. The defects considered in the following examples are: a single flaw, a step flaw, two flaws, and a triple defect shown in Figs.17-20. To employ Model 1 as a reference model to reconstruct a single defect in Fig.21, the reconstruction is less accurate than the one obtained using Model 2. This can be interpreted as the better relatedness to the real defect using Model 2 than the one by Model 1 in terms of the area of the defect. In the step flaw construction example in Fig.22, the predicted profile of a step defect by Model 2 can reflect the real defect with a higher level of precision than the result by Model 1 owing to the same reason described in the single defect case. To further illustrate the powerful capacity of the improved QDFT approach to circumferential multiple defects, multi-defects inspection such as double defects and triple defects, are performed and the reconstruction of defects is shown in Fig.23 and Fig.24, respectively. The results indicate that effective and efficient reconstruction of defects using QDFT approach can be achieved in terms of the accurate position and sizing. Averagely, the predicted profiles of defects by the reference model of Model 1 are more accurate than the ones reconstructed using Model 2. This is because the depth of the defect in the reference Model 1 gets closer to the equivalent depth of the real defects than the defect depth in Model 2. It is concluded that the defect depth of the reference model is a driving factor to precisely reconstruct the multiple circumferential

surface defects rather than the area of the defect.

Summarily, the quantitative detection of circumferential surface defects in circular annulus using improved QDFT approach can be achieved with a high level of accuracy, no matter which reference model will be chosen. However, the closer the defect profile of the reference model gets to the real defect, the better the predicted reconstruction will be obtained. It is noted that the way to select a better reference model for more accurate reconstruction of circumferential surface defects needs to be further explored in the future work, which should consider the relationship between reference models and real defects in terms of key parameters such as, the defect area, the equivalent defect depth, and the equivalent defect length.

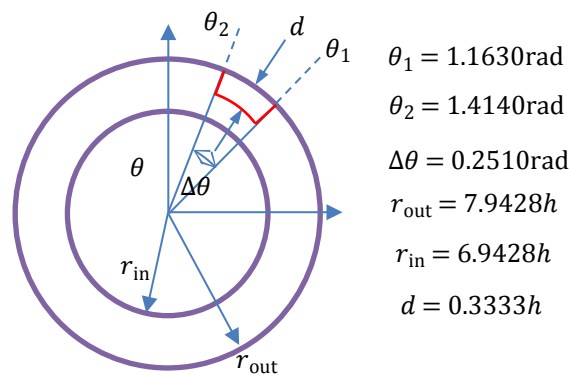


Fig. 17 The circular annulus with single defect

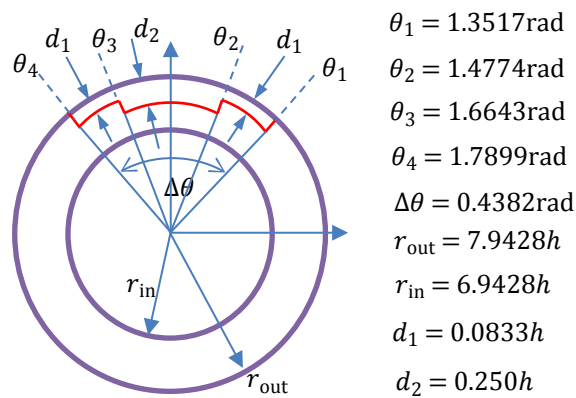


Fig. 18 The circular annulus with a step defect

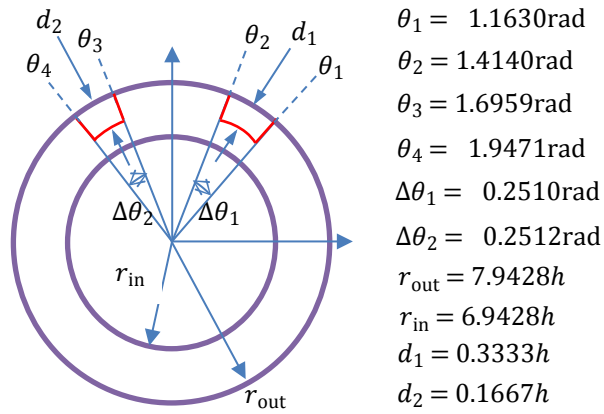


Fig. 19 The circular annulus with double defects

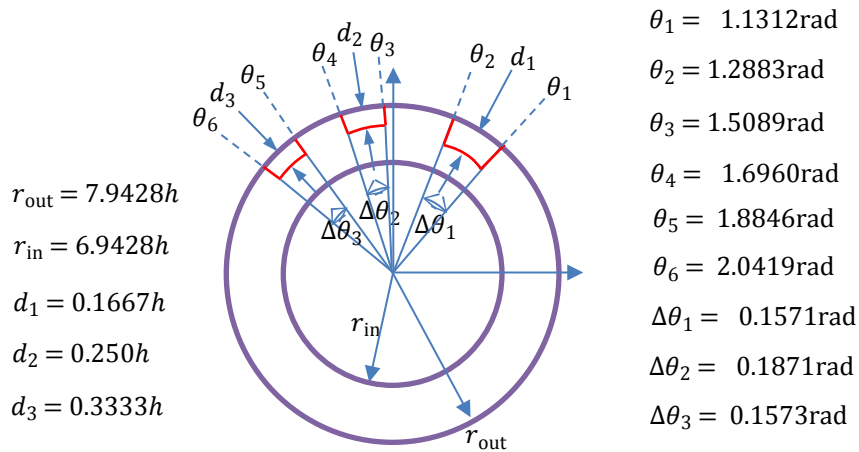


Fig. 20 The circular annulus with triple defects

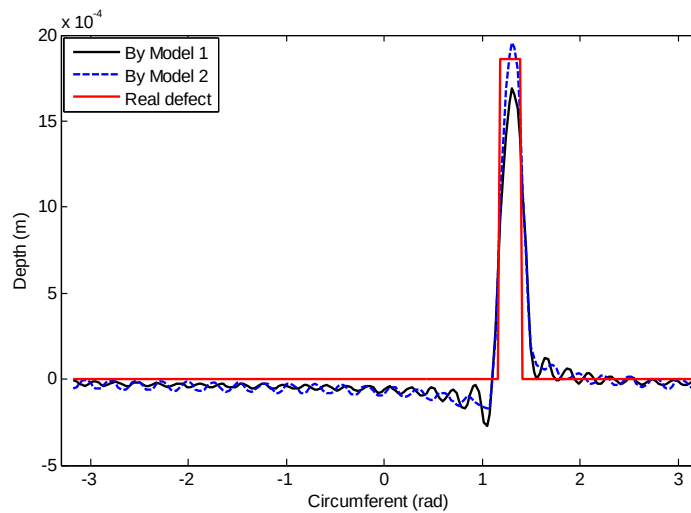


Fig. 21 The reconstructed result of single defect

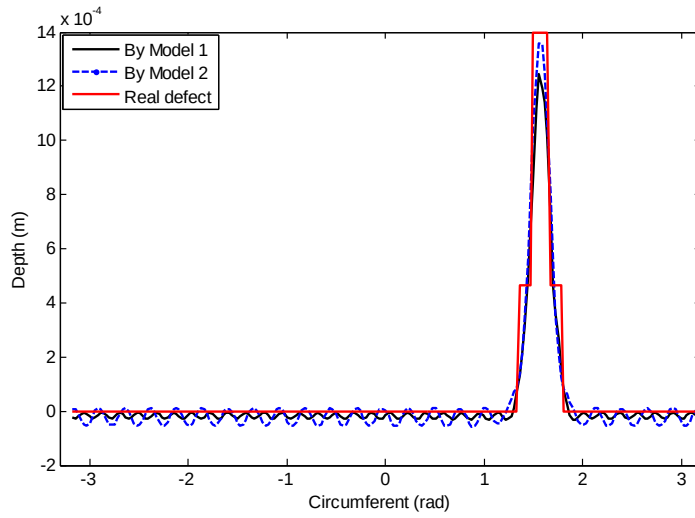


Fig. 22 The reconstructed result of step defect

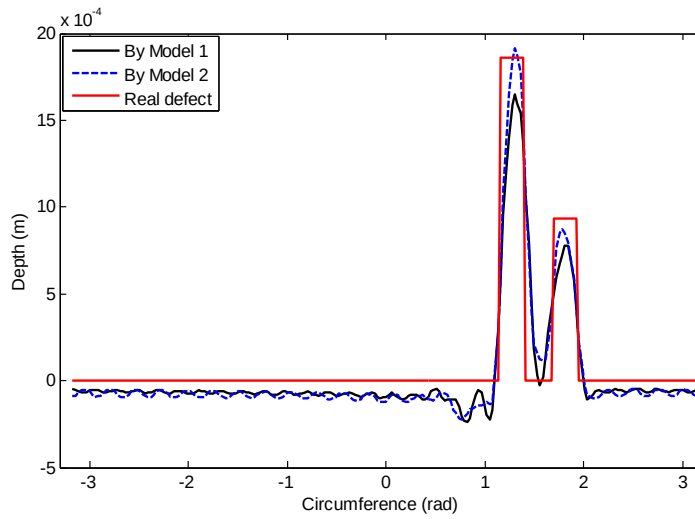


Fig. 23 The reconstructed result of double defects

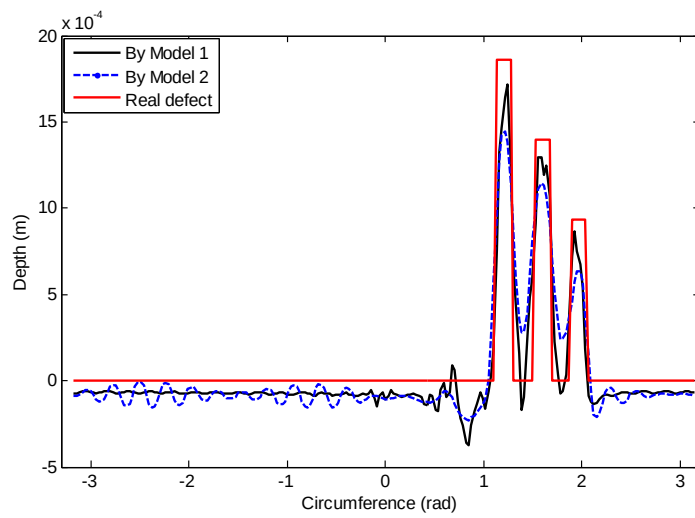


Fig. 24 The reconstructed result of triple defects

5. Conclusion

In this work, the dispersion equations of guided waves propagating along the spiral path of the helix in a hollow cylinder have been derived using the semi-analytical FEM. Based on the theoretical analysis, the scattered fields in circular annulus have been numerically determined by employing the hybrid FEM and also validated by the law of conservation of energy. Through the changes of opening angle and depth of circumferential defects, it is concluded that the peak number and magnitude of the reflection coefficients increase with the opening angle and depth of defects, respectively, in the low frequency range. In the reconstruction simulations, it is found that the circumferential surface defects in pipeline structures can be effectively reconstructed with high levels of accuracy and efficiency by the extended QDFT (quantitative detection of Fourier transform) technique, in which general reference models are adopted to investigate defects sizing. It is emphasized that this reconstruction method is not confined by the defect shape and the number of defects, which has been demonstrated throughout four typical defect reconstruction examples. However, the differences between reference models and real structures, the defect area, and the equivalent opening angle and depth of defects are remarkable factors which influence reconstruction precision and are being considered for further research in various engineering subjects by authors. The results shown in this paper will lay a solid foundation for circumferential defect detection using ultrasonic guided waves as well as highlight some implications which could be considered for early-stage, qualitative inspections of circumferential surface flaws in circular annuli.

Acknowledgements

This research was supported by the National Natural Science Foundation of China (nos. 11502108, 11232007, 51405225, and 11611530686), the Program for New Century Excellent Talents in Universities (no. NCET-12-0625), the Natural Science Foundation of Jiangsu Province (nos. BK20140037 and BK20140808), the Fundamental Research Funds for Central Universities (no. NE2013101), and the project funded by the Priority Academic Program Development of Jiangsu Higher Education Institutions (PAPD). The authors would like to thank many colleagues at Nanjing University of Aeronautics and Astronautics for their valuable suggestions during the preparation of this paper, and the reviewers for their instructive comments on the paper.

References

- [1] Cook, E. G., Valkenburg, H. E., 1954. Surface wave at ultrasonic frequencies. *ASTM, Bull.*, Vol. 3, pp. 81-84.
- [2] Gregory, R. D., 1971. The propagation of Rayleigh waves over curved surfaces at high frequency. *Proc. Cambridge Phil. Soc.*, 70, 103-121.
- [3] Liu, G., Qu, J., 1998. Guided circumferential waves in a circular annulus. *Journal of Applied Mechanics*, 65(2), 424-430.
- [4] Qu, J., Berthelot, Y., Li, Z., 1996. Dispersion of guided circumferential waves in circular annulus. *Review of Progress in Quantitative NDE*, 15, 169-176.
- [5] Rattanawangcharoen, N., 1993. Propagation and scattering of elastic waves in laminated circular cylinders. PhD dissertation, Univ. of Manitoba, Winnipeg, Manitoba, Canada.
- [6] Wang, S., Huang S., Zhao, W., Wei, Z., 2015. 3D modeling of circumferential SH guided waves in pipeline for axial cracking detection in ILI tools. *Ultrasonics*, 56, 325-331.

- [7] Leonard, K. R., Eugene, V. M., Hinders, M. K., 2002. Ultrasonic Lamb wave tomography. *Inverse Problems*, 18, 1795-1808.
- [8] Huthwaite, P., Simonetti, F., 2012. Damage detection through sound speed reconstruction. *AIP Conference Proceedings*, 1430, 777-784.
- [9] Huthwaite, P., 2014. Evaluation of inversion approaches for guided wave thickness mapping, 470, 20140063-20140063.
- [10] Luo, W., Rose, J. L., Kwun, H., 2004. Circumferential shear horizontal wave axial-crack sizing in pipes. *Research in Nondestructive Evaluation*, 15, 149-171.
- [11] Valle, C., Niethammer, M., Qu, J., Jacobs L. J., 2001. Crack Characterization using guided circumferential waves. *Journal of the Acoustical Society of America*, 110, 1282-1290.
- [12] Liu, Z., Xu, Q., Gong, Y., He, C., Wu, B., 2014. A new multichannel time reversal focusing method for circumferential Lamb waves and its applications for defect detection in thick-walled pipe with large-diameter. *Ultrasonics*, 54, 1967-1976.
- [13] Liu, Y., Li, Z., Gong, K., 2012. Detection of a radial crack in annular structures using guided circumferential waves and continuous wavelet transform. *Mechanical Systems and Signal Processing*, 30, 157-167.
- [14] Shivaraj, K., Balasubramaniam, K., Krishnamurthy, C. V., Wadhwan, R., 2008. Ultrasonic Circumferential Guided Wave for Pitting-Type Corrosion Imaging at Inaccessible Pipe-Support Locations. *Journal of Pressure Vessel Technology*, 130, 1030-1036.
- [15] Howard, R., Cegla, F., 2017. On the probability of detecting wall thinning defects with dispersive circumferential guided waves. *NDT & E International*, 86, 73-82.
- [16] Dhayalan, R., Balasubramaniam, K., 2010. A hybrid finite element model for simulation of electromagnetic acoustic transducer (EMAT) based plate waves. *NDT & E International*, 43, 519-526.
- [17] Clough, M., Fleming, M., Dixon, S., 2017. Circumferential Guided Wave EMAT System for Pipeline Screening using Shear Horizontal ultrasound. *NDT & E International*, 86, 20-27.
- [18] Sun, Z., Sun, A., Ju, B., 2018. Guided wave imaging of oblique reflecting interfaces in pipes using common-source synthetic focusing. *Journal of Sound and Vibration*, 420, 1-20.
- [19] Zhuang, W., Shah, A. H., 1999. Elastodynamic Green's function for laminated anisotropic circular cylinders. *Journal of Applied Mechanics*, 66, 665-674.
- [20] Marzani, A., 2008. Time-transient response for ultrasonic guided waves propagating in damped cylinders. *International Journal of Solids and Structures*, 45, 6347-6368.
- [21] Da, Y., Dong, G., Wang, B., Liu, D., Qian, Z., 2018. A novel approach to surface defect detection. *International Journal of Engineering Science*. 133, 181-195.
- [22] Stoyko, D. K., Popplewell, N., Shah, A. H., 2014. Detecting and describing a notch in a pipe using singularities. *International Journal of Solids and Structures*, 51, 2729-2743.
- [23] Biryukov, S. V., Gulyaev, Y. V., Krylov, V. V., Plessky, V. P., 1995. *Surface Acoustic Waves in Inhomogeneous Media*. New York: Springer-Verlag.
- [24] Liu, F., Li, H., Lu, H., 2016. Weak-mode identification and time-series reconstruction from high-level noisy measured data of offshore structures. *Applied Ocean Research*. 56, 92-106.
- [25] Liu, F., Lu, H., Ji, C., 2016. A general frequency-domain dynamic analysis algorithm for offshore structures with asymmetric matrices. *Ocean Engineering*. 125, 272-284.